



OPEN ACCESS

RECEIVED
11 May 2020REVISED
21 July 2020ACCEPTED FOR PUBLICATION
4 August 2020PUBLISHED
8 September 2020Original content from
this work may be used
under the terms of the
[Creative Commons
Attribution 4.0 licence](#).Any further distribution
of this work must
maintain attribution to
the author(s) and the
title of the work, journal
citation and DOI.

PAPER

Multigap superconductivity in the Mo_5PB_2 boron–phosphorus compoundT Shang¹ , W Xie², D J Gawryluk¹ , R Khasanov³, J Z Zhao^{4,5}, M Medarde¹, M Shi⁶,
H Q Yuan^{2,7} , E Pomjakushina¹ and T Shiroka^{3,8} ¹ Laboratory for Multiscale Materials Experiments, Paul Scherrer Institute, CH-5232 Villigen PSI, Switzerland² Center for Correlated Matter and Department of Physics, Zhejiang University, Hangzhou, 310058, People's Republic of China³ Laboratory for Muon-Spin Spectroscopy, Paul Scherrer Institute, CH-5232 Villigen PSI, Switzerland⁴ Co-Innovation Center for New Energetic Materials, Southwest University of Science and Technology, Mianyang, 621010, People's Republic of China⁵ Research Laboratory for Quantum Materials, Singapore University of Technology and Design, Singapore 487372, Singapore⁶ Swiss Light Source, Paul Scherrer Institute, CH-5232 Villigen PSI, Switzerland⁷ Collaborative Innovation Center of Advanced Microstructures, Nanjing, 210093, People's Republic of China⁸ Laboratorium für Festkörperphysik, ETH Zürich, CH-8093 Zürich, SwitzerlandE-mail: tian.shang@psi.ch**Keywords:** multigap, superconductivity, muon-spin rotation and relaxation

Abstract

The tetragonal Mo_5PB_2 compound was recently reported to show superconductivity with a critical temperature up to 9.2 K. In search of evidence for multiple superconducting gaps in Mo_5PB_2 , comprehensive measurements, including magnetic susceptibility, electrical resistivity, heat capacity, and muon-spin rotation and relaxation measurements were carried out. Data from both low-temperature superfluid density and electronic specific heat suggest a nodeless superconducting ground state in Mo_5PB_2 . Two superconducting energy gaps $\Delta_0 = 1.02$ meV (25%) and 1.49 meV (75%) are required to describe the low- T electronic specific-heat data. The multigap features are clearly evidenced by the field dependence of the electronic specific-heat coefficient and the Gaussian relaxation rate in the superconducting state (i.e., superfluid density), as well as by the temperature dependence of the upper critical field. By combining our extensive experimental results with numerical band-structure calculations, we provide compelling evidence of multigap superconductivity in Mo_5PB_2 .

1. Introduction

The T_5M_3 family, where T is a transition or rare-earth metal and M a (post)-transition metal or a metalloid element, features three distinct structural symmetries: orthorhombic Yb_5Sb_3 -type ($Pnma$, no. 62), tetragonal Cr_5B_3 -type ($I4/mcm$, no. 140), and hexagonal Mn_5Si_3 -type ($P6_3/mcm$, no. 193). The tetragonal Cr_5B_3 -type structure is adopted by a broad range of binary and ternary compounds. Among these, the layered ternary compounds of transition metals with boron and silicon (or boron and phosphorus), with a $T_5\text{XB}_2$ stoichiometry ($X = \text{P}$ or Si), exhibit many interesting properties. For example, Co_5SiB_2 exhibits a paramagnetic ground state, found to persist down to liquid He temperature [1]. On the other hand, when T is occupied by other $3d$ metals, such as Mn or Fe, both $T_5\text{SiB}_2$ and $T_5\text{PB}_2$ are ferromagnets with high Curie temperatures. Therefore, currently they are being considered for room-temperature magnetocaloric applications or as rare-earth-free permanent magnets [2–5]. Unlike these high-temperature ferromagnets, the $4d$ and $5d$ compounds Nb_5SiB_2 , Mo_5SiB_2 , and W_5SiB_2 are superconductors, with transition temperatures in the 5 to 8 K range [6–9]. Later on, the Cr_5B_3 -type Ta_5GeB_2 boro-germanide was shown to become a superconductor below $T_c \sim 3.8$ K [10]. Very recently, a new member of the Cr_5B_3 -type series, namely Mo_5PB_2 , was synthesized and shown to exhibit superconductivity (SC) with a critical temperature $T_c = 9.2$ K [11], the highest T_c recorded in this family of compounds. According to electrical resistivity measurements under various applied magnetic fields, its upper critical field, $\mu_0 H_{c2} \sim 1.7$ T, seems to be

much higher than that of Mo_5SiB_2 (0.6 T) or W_5SiB_2 (0.5 T) [7, 8]. In addition, over a wide temperature range, the temperature-dependent $H_{c2}(T)$ of Mo_5PB_2 seems inconsistent with the Ginzburg–Landau- or Werthamer–Helfand–Hohenberg models, implying multiple superconducting gaps in Mo_5PB_2 [11]. To date, a detailed analysis of the $H_{c2}(T)$ data is still missing. Yet, possible multigap features were already suggested by zero-field heat-capacity measurements and electronic band-structure calculations [11]. Indeed, its zero-field specific-heat seems more consistent with a two-gap- rather than with a single-gap model, as confirmed also by the present work. First-principle calculations indicate Mo_5PB_2 to be a multiband metal, whose density of states (DOS) at the Fermi level is dominated by the Mo 4*d*-orbitals. Although electronic band-structure calculations are available for Mo_5PB_2 and its superconductivity has been studied via macroscopic techniques (e.g., specific heat), the microscopic nature of its SC remains largely unexplored. In particular, the multigap feature of Mo_5PB_2 demands stronger evidence. To this aim, we performed an extensive study of the superconducting properties of Mo_5PB_2 by means of electrical resistivity, magnetization, thermodynamic- and, in particular, by muon-spin rotation and relaxation (μSR) methods. We find that Mo_5PB_2 exhibits a fully-gapped superconducting state with preserved time-reversal symmetry. Its multigap features are strongly evidenced by the field-dependent electronic specific-heat coefficient, as well as by the superconducting μSR relaxation, the latter being highly consistent with the temperature dependence of the upper critical field.

2. Methods

Polycrystalline samples of Mo_5PB_2 were prepared by solid-state reaction methods, the procedures used to synthesize the material being reported in detail elsewhere [11]. Room-temperature x-ray powder diffraction (XRD) measurements were used to check the quality of the Mo_5PB_2 samples, by employing a Bruker D8 diffractometer with Cu $K\alpha$ radiation. The magnetic susceptibility, electrical resistivity, and heat-capacity measurements were performed on a 7-T Quantum Design magnetic property measurement system (MPMS-7) and a 14-T physical property measurement system (PPMS-14) equipped with a ^3He cryostat.

The bulk μSR measurements were carried out at the general-purpose and the multipurpose (Dolly) surface-muon spectrometers at the Swiss muon source of Paul Scherrer Institute, Villigen, Switzerland [12]. For the low-temperature measurements on Dolly (down to ~ 0.3 K), the samples were mounted on a thin copper foil (ca ~ 30 μm thick) using diluted GE varnish. Transverse-field (TF) μSR measurements were carried out to investigate the superconducting properties (mostly the gap symmetry) of Mo_5PB_2 . To track the additional field-distribution broadening due to the flux-line-lattice (FLL) in the mixed superconducting state, we followed a field-cooling (FC) protocol, where the magnetic field is applied in the normal state, before cooling the sample down to base temperature. Afterwards, the TF- μSR spectra were collected at various temperatures upon warming. The μSR data were analyzed by means of the *muSRfit* software package [13].

The electronic band structure of Mo_5PB_2 was calculated via the density functional theory, within the generalized gradient approximation of Perdew–Burke–Ernzerhof realization [14], as implemented in the Vienna *ab initio* simulation package [15, 16]. The projector augmented wave pseudopotentials were adopted for the calculation [17, 18]. Electrons belonging to the outer atomic configuration were treated as valence electrons, here corresponding to 6 electrons in Mo ($4d^5 5s^1$), 5 electrons in P ($3s^2 3p^3$), and 3 electrons in B ($2s^2 2p^1$). The kinetic energy cutoff was fixed to 500 eV. The lattice parameters and the atomic positions experimentally determined from Rietveld refinements were chosen for the calculations. For the self-consistent calculation, the Brillouin zone integration was performed on a Γ -centered mesh of $10 \times 10 \times 10$ k -points.

3. Results and discussion

3.1. Crystal structure and phase purity

The crystal structure and the purity of Mo_5PB_2 polycrystalline samples were checked via powder XRD at room temperature. Figure 1 shows a refinement of the XRD pattern, performed by means of the FullProf Rietveld-analysis suite [19]. The refinement confirms that Mo_5PB_2 crystallizes in the tetragonal Cr_5B_3 -type structure, also known as T_2 -phase. The refined lattice parameters, $a = b = 5.971\,05(5)$ Å and $c = 11.070\,08(11)$ Å, are in good agreement with the results reported in the literature [11]. Similar to previous work, also our data (see figure 1) indicate that, besides the main Mo_5PB_2 phase (80%), there are also extra reflections belonging to minor foreign phases: Mo_3P (16%) and $\text{MoB}/\text{Mo}_2\text{B}$ (4%). Once formed, due to their very high melting temperature (above 2000 °C), such extraneous phases are very stable and almost impossible to remove, even after multiple additional annealings. These minor phases, too, are

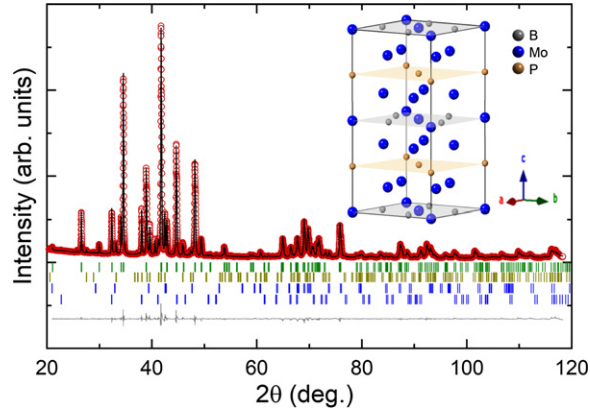


Figure 1. Room-temperature x-ray powder diffraction pattern and Rietveld refinement for Mo_5PB_2 . The red circles and the solid black line represent the experimental pattern and the Rietveld refinement profile, respectively. The gray line at the bottom shows the residuals, i.e., the difference between calculated and experimental data. The vertical bars mark the calculated Bragg-peak positions for Mo_5PB_2 (green), Mo_3P (yellow), and $\text{MoB}/\text{Mo}_2\text{B}$ (blue). The crystal structure (unit cell) is shown in the inset.

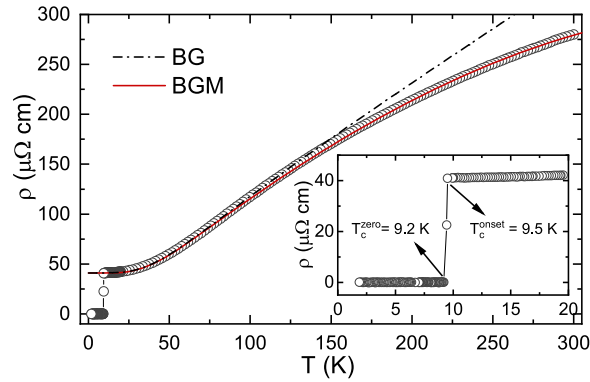


Figure 2. Temperature dependence of the electrical resistivity of Mo_5PB_2 collected in zero field up to room temperature. The black dash-dotted and red solid lines through the data are fits to the Bloch–Grüneisen formula with (BGM) and without (BG) Mott correction, respectively. The inset shows a closeup of the low-temperature region, highlighting the superconducting transition.

superconductors, with critical temperatures below 5.5 K [20–22]. Nevertheless, upon investigating the Mo_5PB_2 samples, no superconducting signal from the MoB or Mo_2B phases could be identified. Therefore, they do not influence the determination of the superconducting parameters of Mo_5PB_2 . As for Mo_3P , its contribution was properly subtracted when analyzing the zero-field specific-heat data (see details below and in reference [11]). The refined Mo_5PB_2 crystal structure, shown in the inset, comprises three different layers (MoB , Mo , and P), stacked alternatively along the c -axis and resembling a quasi-two dimensional structure. Clearly, in the unit cell there are two distinct crystallographic sites for the Mo atoms and a single site for the P or B atoms.

3.2. Electrical resistivity

The temperature dependence of the electrical resistivity $\rho(T)$, collected in zero magnetic field from 300 down to 2 K, reveals the metallic character of Mo_5PB_2 (see figure 2). The electrical resistivity in the low- T region is shown in the inset. Here, the superconducting transition, with $T_c^{\text{onset}} = 9.5$ K and $T_c^{\text{zero}} = 9.2$ K, is clearly visible and the data are consistent with previous work [11]. The normal-state electrical resistivity is well modeled by the Bloch–Grüneisen–Mott (BGM) formula

$$\rho(T) = \rho_0 + 4A(T/\Theta_D^R)^5 \int_0^{\Theta_D^R/T} \frac{z^5 dz}{(e^z - 1)(1 - e^{-z})} - \alpha T^3$$
 [23, 24]. Here, ρ_0 represents the residual resistivity, while the second term describes the electron–phonon scattering, with Θ_D^R being the characteristic Debye temperature and A a coupling constant. The third term represents a contribution from the s – d interband scattering, α being the Mott coefficient [25, 26]. As shown in figure 2, the Mott correction is clearly required. Indeed, the black dash-dotted line, a fit to the BG formula without the Mott term, deviates significantly from the experimental data above 150 K. The fit to BGM (red solid line) results in $\rho_0 = 41.1(2) \mu\Omega \text{ cm}$, $A = 250(8) \mu\Omega \text{ cm}$, $\Theta_D^R = 236(5) \text{ K}$, and $\alpha = 2.2(1) \times 10^{-6} \mu\Omega \text{ cm K}^{-3}$. A similar α

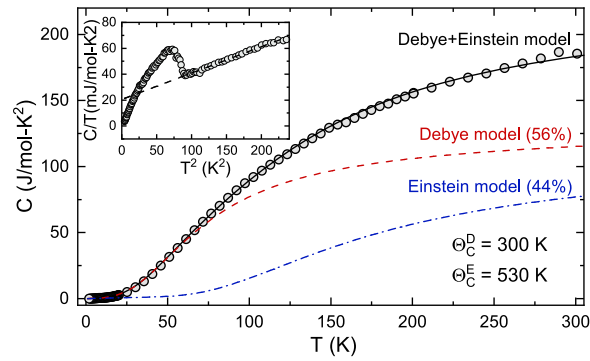


Figure 3. Temperature dependence of the Mo_5PB_2 heat capacity, measured in zero field from 2 to 300 K. The solid line represents a fit to a combined Debye- and Einstein model, with the dashed- and dash-dotted lines referring to the two components. Inset: specific heat C/T vs T^2 in the low- T regime; the dashed-line is a fit to $C/T = \gamma_n + \beta T^2 + \delta T^4$, where γ_n is the electronic specific-heat coefficient, while the two other terms account for the phonon contribution to the specific heat. The determined values are $\gamma_n = 22.3(2) \text{ mJ mol}^{-1} \text{ K}^{-2}$, $\beta = 0.17(3) \text{ mJ mol}^{-1} \text{ K}^{-4}$ and $\delta = 1.3(9) \times 10^{-4} \text{ mJ mol}^{-1} \text{ K}^{-6}$.

value was also found in Mo_3P ($3.4 \mu\Omega \text{ cm K}^{-3}$) [22], indicating that, most likely, the s - d scattering is due to Mo d - and to P s -electrons.

3.3. Heat capacity

The Debye temperature can also be estimated from the heat capacity measurements. As shown in figure 3, a pure Debye model cannot fit the $C(T)$ data properly. However, when combined with an Einstein model, it reproduces the $C(T)$ data fairly accurately. In this case, the solid line is a fit to the Debye- and Einstein model $C(T) = \gamma_n T + n[vC_D(T) + (1-v)C_E(T)]$, with relative weights v and $(1-v)$. Here, $n = 8$ is the number of atoms per formula-unit in Mo_5PB_2 . The first term represents the electronic specific heat, which can be extracted from the low- T data (see inset in figure 3). The second and the third terms represent the acoustic- and optical phonon-mode contributions, described by the Debye-

$$C_D(T) = 9R(T/\Theta_D^C)^3 \int_0^{\Theta_D^C/T} \frac{z^4 dz}{(e^z - 1)^2} \text{ and Einstein model } C_E(T) = 3R(\Theta_E^C/T)^2 \frac{\exp(\Theta_E^C/T)}{[\exp(\Theta_E^C/T) - 1]^2}, \text{ respectively [27].}$$

Here $R = 8.314 \text{ J mol}^{-1} \text{ K}^{-1}$ is the molar gas constant, while Θ_D^C and Θ_E^C are the Debye and Einstein temperatures. The solid line in figure 3 represents the best fit, corresponding to $\Theta_D^C = 300(5) \text{ K}$, $\Theta_E^C = 530(5) \text{ K}$, and $v = 0.56$. The obtained Debye temperature is slightly higher than that derived from electrical resistivity data (see figure 2). In fact, unlike electrical transport, heat capacity reflects better the bulk properties and, therefore, is more susceptible to extrinsic phases. In our case, the higher Debye temperature determined from heat-capacity measurements is most likely related to the MoB or Mo_2B phases, since the light B atoms usually exhibit rather high phonon frequencies, corresponding to large Debye temperatures (e.g., $\Theta_D \sim 400 \text{ K}$ for MoB) [28].

3.4. Magnetization

The superconductivity of Mo_5PB_2 was also evidenced by magnetization measurements. The temperature-dependent magnetic susceptibility $\chi(T)$ measured in a field of 1 mT using both field-cooled and zero-field-cooled (ZFC) protocols, is shown in figure 4(a). A sharp diamagnetic transition at $T_c = 9.3 \text{ K}$ indicates the onset of superconductivity in Mo_5PB_2 , in agreement with the values determined from electrical resistivity and heat capacity. The well separated ZFC- and FC-susceptibility curves imply a strong flux-pinning effect in Mo_5PB_2 . By assuming a cuboid (or, in general, an ellipsoid) sample shape with $a/b \sim 1$ and $c/a \sim 0.5$, the estimated demagnetization factor is ~ 0.5 , with the field applied along the c -direction [29, 30]. After accounting for the demagnetization factor, the superconducting shielding fraction of Mo_5PB_2 is about 92%. To determine the lower critical field $\mu_0 H_{c1}$ of Mo_5PB_2 , essential for performing μSR measurements on type-II superconductors, the field-dependent magnetization $M(H)$ was measured at various temperatures up to T_c . Some representative $M(H)$ curves, recorded using a ZFC-protocol, are shown in the inset of figure 4(b). The estimated $\mu_0 H_{c1}$ values vs temperature are summarized in the main panel, where the zero-temperature lower critical field $\mu_0 H_{c1}(0) = 30.4(4) \text{ mT}$ is also determined. This is highly consistent with 30.8 mT, the value calculated from the magnetic penetration depth λ_0 (see below).

3.5. TF- μSR and superconducting order parameter

The TF- μSR measurements were carried out in a field of 80 mT, twice the $\mu_0 H_{c1}(0)$ value. Two representative TF- μSR spectra of Mo_5PB_2 , collected at 0.3 K and 10 K (i.e., in the superconducting

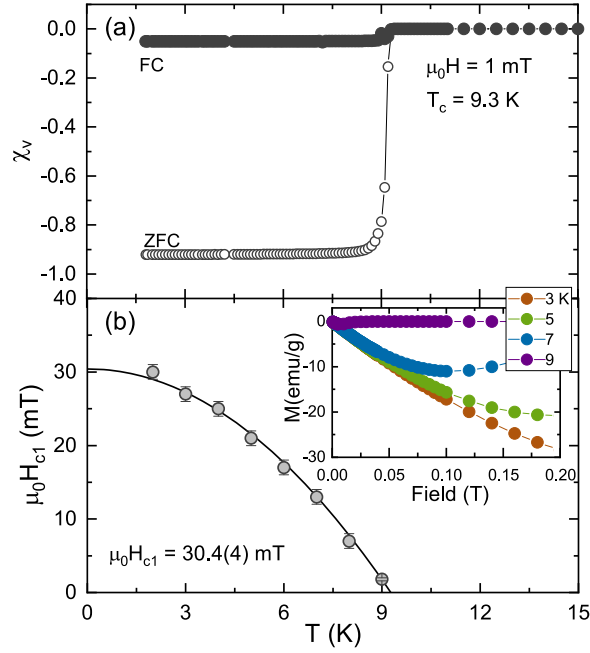


Figure 4. (a) Temperature-dependent magnetic susceptibility of Mo_5PB_2 , measured in an applied field of 1 mT using the ZFC- and FC protocols. (b) Estimated lower critical field $\mu_0 H_{c1}$ vs temperature. The solid line is a fit to the phenomenological equation $\mu_0 H_{c1}(T) = \mu_0 H_{c1}(0)[1 - (T/T_c)^2]$. The inset shows representative field-dependent magnetization curves $M(H)$ recorded at various temperatures up to T_c . For each temperature, the lower critical field $\mu_0 H_{c1}$ was determined as the magnetic field where the diamagnetic response deviates from the linear relation vs the magnetic field.

and the normal state) are shown in figure 5(a). In the normal state, the spectra have essentially no damping, reflecting the uniform field distribution, as well as the nonmagnetic nature of Mo_5PB_2 . Below T_c , instead, the significantly enhanced damping occurring in the mixed state reflects the inhomogeneous field distribution due to the development of FLL [31–34]. This additional SC-related broadening is clearly visible in figure 5(b), where the fast-Fourier-transform spectrum of the corresponding TF- μSR data is shown. To describe the asymmetric field distribution taking place below T_c , the μSR spectra can be modeled by means of the expression:

$$A_{\text{TF}}(t) = \sum_{i=1}^n A_i \cos(\gamma_\mu B_i t + \phi) e^{-\sigma_i^2 t^2 / 2} + A_{\text{bg}} \cos(\gamma_\mu B_{\text{bg}} t + \phi). \quad (1)$$

Here A_i and A_{bg} represent the initial muon-spin asymmetries for muons implanted in the sample and sample holder, respectively, with the latter giving rise to a background signal not undergoing any depolarization. B_i and B_{bg} are the local fields sensed by the implanted muons in the sample and the sample holder (the latter normally experiencing the unchanged external field), $\gamma_\mu/2\pi = 135.53 \text{ MHz T}^{-1}$ is the muon gyromagnetic ratio, ϕ is a shared initial phase, and σ_i is the Gaussian relaxation rate of the i th component.

Generally, the field distribution in the SC state is material dependent: the more asymmetric it is, the more components are required to describe it. Here we found that, to properly describe the TF- μSR spectra in the superconducting state of Mo_5PB_2 , at least two oscillations are required. This is illustrated in figure 5(b), where two broad peaks, above and below the applied magnetic field (80 mT), can be clearly seen. Both peaks are much broader than the single peak shown in figure 5(c), corresponding to the field distribution in the normal state. The solid lines in figure 5 represent fits to equation (1) with $n = 2$, while the dash-dotted lines in figure 5(b) evidence the single components at 0.3 K and the background signal. The derived Gaussian relaxation rates as a function of temperature are summarized in the inset of figure 6. At base temperature (0.3 K), $\sigma_1 = 7.72(16) \mu\text{s}^{-1}$ and $\sigma_2 = 2.32(10) \mu\text{s}^{-1}$ reflect the A_1 and A_2 field distributions in figure 5(b), respectively. Above T_c , the relaxation rate is small and temperature-independent, but below T_c it starts to increase due to the onset of FLL and the increased superfluid density. At the same time, also a diamagnetic field shift appears below T_c , given by $\Delta B(T) = \langle B \rangle - B_{\text{appl}}$, with $\langle B \rangle = (A_1 B_1 + A_2 B_2)/A_{\text{tot}}$, $A_{\text{tot}} = A_1 + A_2$, and $B_{\text{appl}} = 80 \text{ mT}$ (see inset in figure 6). The effective Gaussian relaxation rate can be estimated from $\sigma_{\text{eff}}^2/\gamma_\mu^2 = \sum_{i=1}^2 A_i [\sigma_i^2/\gamma_\mu^2 - (B_i - \langle B \rangle)^2]/A_{\text{tot}}$ [34]. Then, the superconducting Gaussian relaxation

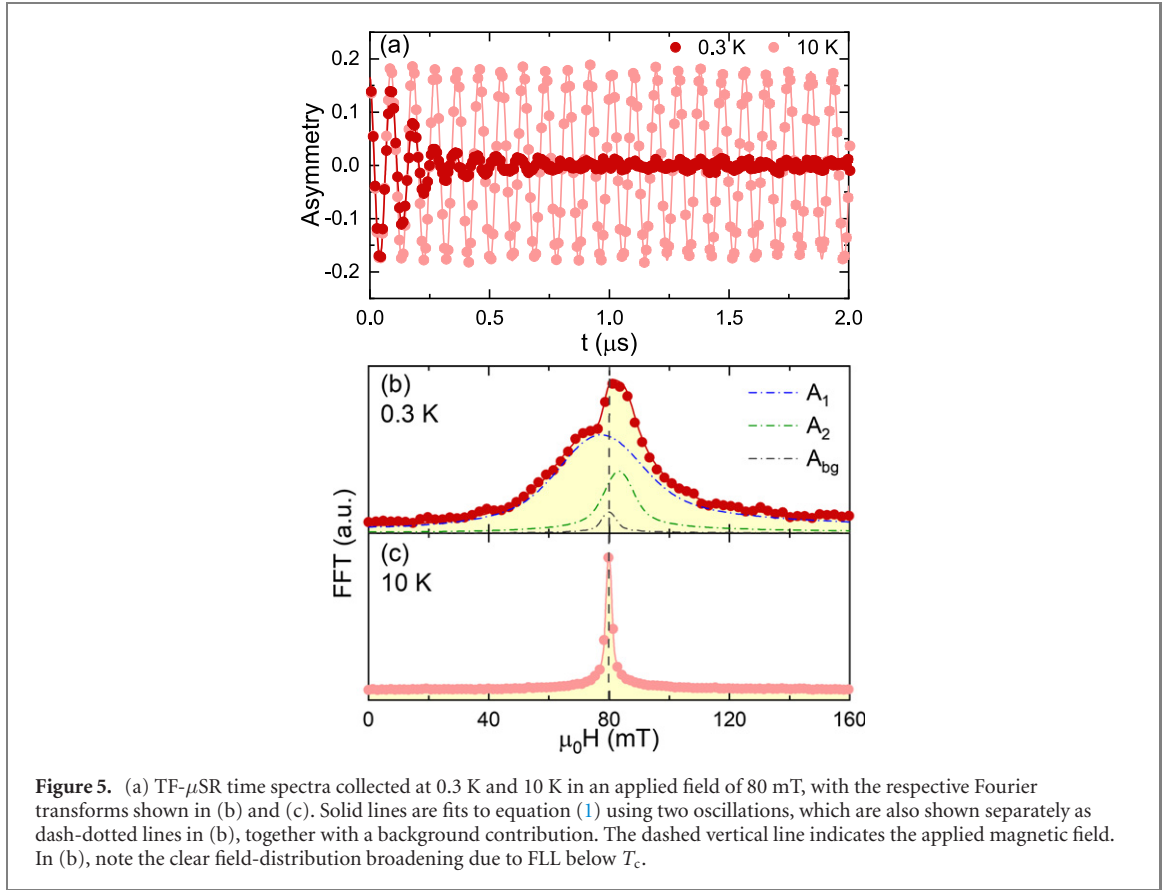


Figure 5. (a) TF-μSR time spectra collected at 0.3 K and 10 K in an applied field of 80 mT, with the respective Fourier transforms shown in (b) and (c). Solid lines are fits to equation (1) using two oscillations, which are also shown separately as dash-dotted lines in (b), together with a background contribution. The dashed vertical line indicates the applied magnetic field. In (b), note the clear field-distribution broadening due to FLL below T_c .

rate, encoded in the σ_{FLL} value, can be extracted by subtracting the nuclear contribution according to $\sigma_{\text{FLL}} = \sqrt{\sigma_{\text{eff}}^2 - \sigma_n^2}$. Here, $\sigma_n \sim 0.11 \mu\text{s}^{-1}$ is the nuclear relaxation rate, almost constant in our narrow temperature range, as confirmed by zero-field (ZF) μSR data (see figure 12). For small applied magnetic fields ($H_{\text{appl}}/H_{c2} \sim 0.04 \ll 1$), the magnetic penetration depth λ can be calculated from $\sigma_{\text{sc}}^2(T)/\gamma_\mu^2 = 0.00371\Phi_0^2/\lambda^4(T)$ [35, 36]. Figure 6 shows the temperature dependent inverse square of the magnetic penetration depth [proportional to the superfluid density, i.e., $\lambda^{-2}(T) \propto \rho_{\text{sc}}(T)$] for Mo_5PB_2 . The superfluid density $\rho_{\text{sc}}(T)$ was further analyzed by using different models, generally described by:

$$\rho_{\text{sc}}(T) = 1 + 2 \left\langle \int_{\Delta_k}^{\infty} \frac{E}{\sqrt{E^2 - \Delta_k^2}} \frac{\partial f}{\partial E} dE \right\rangle_{\text{FS}}. \quad (2)$$

Here, $f = (1 + e^{E/k_B T})^{-1}$ is the Fermi function and $\langle \rangle_{\text{FS}}$ represents an average over the Fermi surface [37]. $\Delta_k(T) = \Delta(T)\delta_k$ is an angle-dependent gap function, where Δ is the maximum gap value and δ_k is the angular dependence of the gap, equal to 1, $\cos 2\phi$, and $\sin \theta$ for an s -, d -, and p -wave model, respectively, with ϕ and θ being the azimuthal angles. The temperature dependence of the gap is assumed to follow $\Delta(T) = \Delta_0 \tanh\{1.82[1.018(T_c/T - 1)]^{0.51}\}$ [37, 38], where Δ_0 is the gap value at 0 K.

Four different models, including single-gap s -, p -, and d -wave, and two-gap $s + s$ -wave, were used to describe the $\lambda^{-2}(T)$. For an s - or p -wave model, the best fits yield the same zero-temperature magnetic penetration depth $\lambda_0 = 121(2)$ nm, but different gap values, 1.42(2) and 1.87(2) meV, respectively. For the d -wave model, the estimated λ_0 and gap value are 104(2) nm and 1.75(2) meV. As can be clearly seen in figure 6, the significant deviation of the p - or d -wave model from the experimental data below 5 K and the temperature-independent behavior of $\lambda^{-2}(T)$ for $T < 1/3T_c \sim 3$ K strongly suggest a fully-gapped superconductivity in Mo_5PB_2 . According to previous studies [11], two gaps are required to quantitatively describe the specific-heat data (as confirmed also here). Here, by fixing the weight $w = 0.25$, as determined from the electronic specific heat (see below), the two-gap $s + s$ -wave model provides almost identical results to the single-gap s -wave model. The two derived gap values $\Delta_0^f = 1.11(2)$ and $\Delta_0^s = 1.57(1)$ meV are very similar to those determined from electronic specific heat.

Since the weight of the second gap is relatively small (0.25–0.3) and the gap sizes are not significantly different ($\Delta_0^f/\Delta_0^s \sim 0.71$), this makes it difficult to discriminate between a single- and a two-gap superconductor based on the temperature-dependent superfluid density alone [39, 40]. Nevertheless,

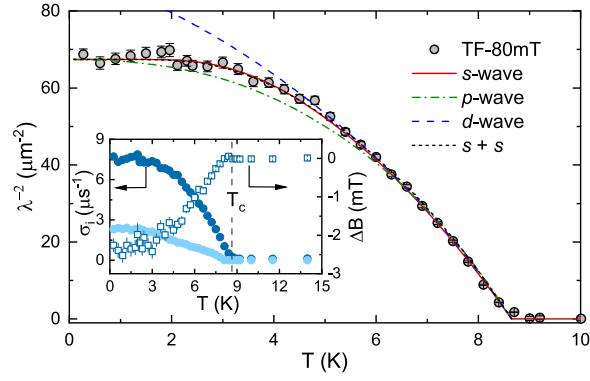


Figure 6. Superfluid density vs temperature, as determined from TF- μ SR measurements in Mo_5PB_2 in an applied magnetic field of 80 mT. The inset shows the temperature dependence of the muon-spin relaxation rate $\sigma_i(T)$ and diamagnetic shift $\Delta B(T) = \langle B \rangle - B_{\text{appl}}$. Two σ s are required to describe the TF- μ SR data [see figure 5(b)]. The different lines in the main panel represent fits to various models, including single-gap s -, p -, and d -wave, and two-gap $s + s$ -wave (see text for details). Note that, after subtracting a possible Mo_3P contribution in quadrature, the resulting data practically overlap with the originally measured $\lambda^{-2}(T)$.

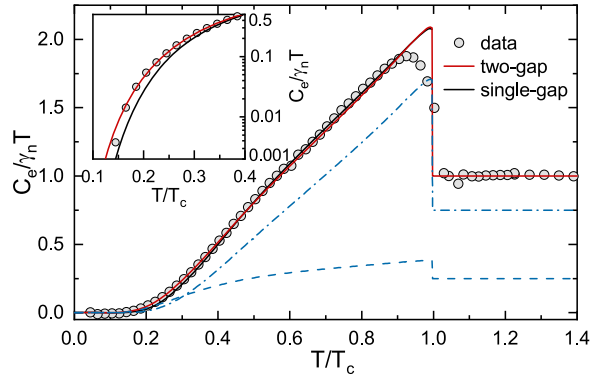


Figure 7. Normalized electronic specific heat $C_e/\gamma_n T$ of Mo_5PB_2 as a function of T/T_c . Inset: enlarged plot of the low- T ($0.1 \leq T/T_c \leq 0.4$) normalized electronic specific heat in semi-logarithmic scale. The solid red and black lines represent the electronic specific heat calculated by considering a fully-gapped s -wave model with two gaps or a single gap, respectively. The dash-dotted- and dashed blue lines in the main panel represent the individual contributions from the large and small superconducting gaps. The goodness of fit is $\chi_r^2 = 1.9$ (two-band model) and 7.9 (single-band model).

as we show further, the two-gap feature of Mo_5PB_2 is clearly reflected also in its field-dependent superconducting relaxation rate $\sigma_{\text{FLL}}(H)$. Since normally the different gaps respond differently to an external field, $\sigma_{\text{FLL}}(H)$ exhibits different features in a two-gap superconductor compared to a single-gap superconductor.

To reveal the multigap superconductivity of Mo_5PB_2 , we also analyzed the zero-field electronic specific-heat data. After subtracting from the raw specific-heat data the phonon contribution (see details in the inset of figure 3) and the spurious Mo_3P contribution (see details in reference [11]), the resulting electronic specific heat divided by the normal-state electronic specific-heat coefficient, i.e., $C_e/\gamma_n T$, is reported in figure 7. Since the previous analysis of $\lambda^{-2}(T)$ already excluded the occurrence of nodes in the SC gap, the temperature-dependent electronic specific heat was analyzed by using a fully-gapped model. The solid black line in figure 7 represents a fit to the s -wave model with a single gap $\Delta_0 = 1.38(2)$ meV (i.e., equivalent to the standard BCS value $1.76k_B T_c$). It reproduces very well the experimental data above $T/T_c \sim 0.4$. Yet, at lower temperatures, the single-gap model shows a less satisfactory agreement (see inset). At the same time, the two-gap model exhibits a much better agreement across the full temperature range, in particular for $T/T_c < 0.4$ (see inset), reflected in a much smaller χ_r^2 value. The solid red line in figure 7 is a fit to the two-gap s -wave model, $C_e(T)/T = wC_e^{\Delta^f}(T)/T + (1-w)C_e^{\Delta^s}(T)/T$ [41]. Here $C_e^{\Delta^f}(T)/T$ and $C_e^{\Delta^s}(T)/T$ are the single-gap specific-heat contributions, with Δ^f the first- (small) and Δ^s the second (large) gap, and w the relative weight. The two-gap model gives $\Delta_0^f = 1.02(2)$ meV, $\Delta_0^s = 1.49(2)$ meV, and $w = 0.25$, the two superconducting gap values being consistent with previous results [11]. The large-gap value, as well as the gap value determined from TF- μ SR, are both greater than Δ_{BCS} expected from the BCS theory in the weak-coupling regime, hence indicating *strong-coupling* superconductivity in Mo_5PB_2 .

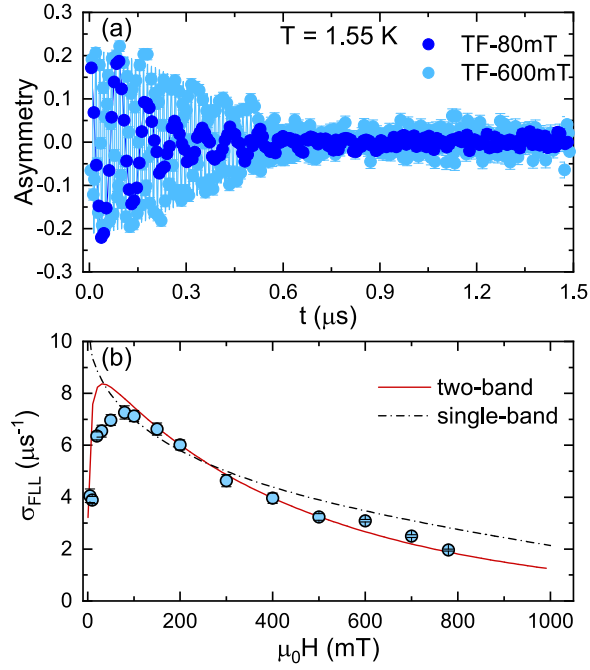


Figure 8. (a) TF- μ SR time spectra for Mo_5PB_2 measured in the superconducting state ($T = 1.55$ K) in a field of 80 and 600 mT. (b) Field-dependent superconducting Gaussian relaxation rate $\sigma_{\text{FLL}}(H)$. The solid and dash-dotted lines represent fits to two-band and single-band models, respectively. The poor agreement between theory and experiment below H_{c1} reflects the magnetic field expulsion from the sample due to the Meissner effect.

3.6. Field-dependent measurements: evidence of multigap superconductivity

To get further insight into the multigap SC revealed by zero-field electronic specific heat, we also carried out a series of measurements (including TF- μ SR, heat capacity, magnetization, and electrical resistivity) at different magnetic fields. The later three were also used to determine the upper critical field $H_{c2}(T)$.

σ_{FLL} vs H . TF- μ SR measurements at different magnetic fields (up to 780 mT) were performed in the superconducting state of Mo_5PB_2 . As an example, the TF- μ SR spectra collected at 80 and 600 mT are shown in figure 8(a). Again the spectra were analyzed using the model described by equation (1). The resulting superconducting Gaussian relaxation rates σ_{FLL} versus the applied magnetic field are summarized in figure 8(b). In case of a single-gap superconductor, $\sigma_{\text{FLL}}(H)$ generally follows $\sigma_{\text{FLL}} = 0.172 \frac{\gamma_{\mu} \Phi_0}{2\pi} (1-h)[1 + 1.21(1-\sqrt{h})^3] \lambda^{-2}$ [35, 36], where $h = H_{\text{appl}}/H_{c2}$, with H_{appl} being the applied magnetic field. By fixing $\mu_0 H_{c2} = 1.77$ T (at 1.55 K) (see figure 10), the single-band model clearly deviates from the experimental data at magnetic fields above 300 mT [see dash-dotted line in figure 8(b)]. In a two-band model, each band is characterized by its own coherence length [i.e., ξ^f (first) and ξ^s (second)] and a weight w [or $(1-w)$], accounting for the relative contribution of each band to the total σ_{FLL} and, hence, to the superfluid density [39, 42]. By fixing $w = 0.25$, as estimated from electronic specific-heat data (figure 7), the two-band model [solid red line in figure 8(b)] is in better agreement with the experiment and provides $\lambda_0 = 99(2)$ nm, $\xi^f = 18.5(5)$ nm, and $\xi^s = 13.2(2)$ nm. The upper critical field of 1.89(5) T, calculated from the coherence length of the second band, $\mu_0 H_{c2} = \Phi_0/(2\pi\xi^2)$, is also comparable to the upper critical field determined from bulk measurements. The *virtual* upper critical field $\mu_0 H_{c2}^* = 0.96(5)$ T, calculated from the coherence length of the first band ξ^f , is in good agreement with the field value where both $H_{c2}(T)$ (figure 10) and $\gamma_{\text{H}}(H)$ (figure 11) show a flex or change the slope, respectively.

Upper critical field. The upper critical field H_{c2} of Mo_5PB_2 was determined from measurements of the electrical resistivity $\rho(T, H)$, magnetization $M(T, H)$, and specific heat $C(T, H)/T$ under various applied magnetic fields up to 2.5 T, as shown in figures 9(a)–(c). Under applied field, the superconducting transition shifts towards lower temperatures and becomes broader. The H_{c2} values, determined using different techniques, are highly consistent and are summarized in figure 10 as a function of the reduced temperature $T_c/T_c(0)$ [here, $T_c(0)$ is the transition temperature in zero field]. The $H_{c2}(T)$ was analyzed by means of Ginzburg–Landau (GL) [43], Werthamer–Helfand–Hohenberg (WHH) [44], and two-band (TB) models [45]. As shown in the inset of figure 10, the GL model reproduces the experimental data up to $\mu_0 H \sim 1.4$ T, while the WHH model stops already at 0.5 T. At higher magnetic fields, both models show large deviations, leading to underestimated values of $\mu_0 H_{c2}^{\text{GL}}(0) = 1.7(1)$ T and $\mu_0 H_{c2}^{\text{WHH}}(0) = 1.3(1)$ T.

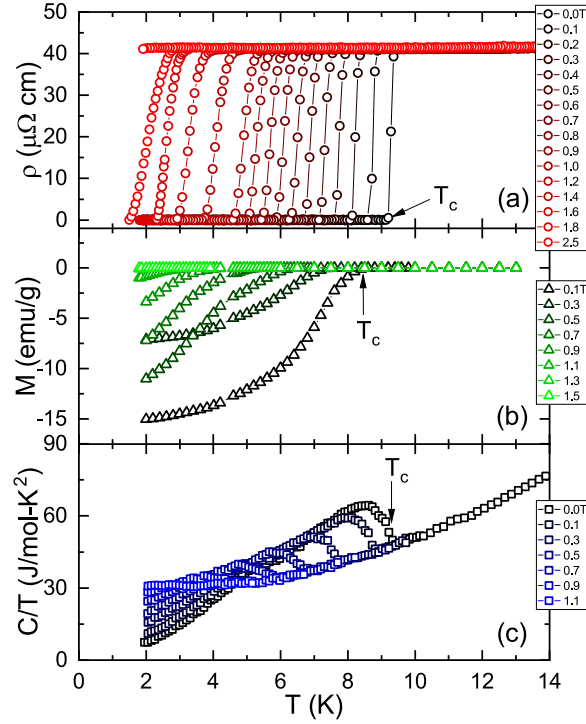


Figure 9. Temperature-dependent (a) electrical resistivity $\rho(T, H)$, (b) magnetization $M(T, H)$, and (c) specific-heat data $C(T, H)/T$, collected at various magnetic fields up to 2.5 T. For the $\rho(T, H)$ measurements, T_c was defined as the onset of zero resistivity; while for the $M(T, H)$ and $C(T, H)/T$ measurements, T_c was defined as the onset and the midpoint of the superconducting transition, respectively. All $T_c(0)$ values are marked by arrows.

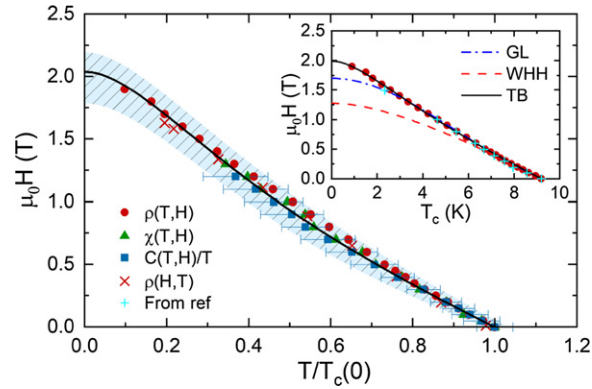


Figure 10. (a) Upper critical field $\mu_0 H_{c2}$ vs reduced transition temperature $T_c/T_c(0)$ for Mo₅PB₂. The T_c values were determined from measurements shown in figure 9. Inset shows the critical field vs T_c , as determined from $\rho(T, H)$ and data taken from reference [11]. Three different fits, using the GL- (dash-dotted line), WHH- (dashed line), and TB model (solid line) are also shown in the inset. The error bars are determined as the superconducting transition widths ΔT_c in the specific-heat data. The shaded region indicates the upper- and lower- H_{c2} limits, as determined using the two-band model.

Such discrepancy most likely hints at multiple superconducting gaps in Mo₅PB₂, as evidenced also by the positive curvature of $H_{c2}(T)$ at low fields, a typical feature of multigap superconductors, as e.g., MgB₂ [46, 47] or Lu₂Fe₃Si₅ [48]. As shown in figure 10, around $T_c/T_c(0) \sim 0.5$ ($\mu_0 H \sim 0.93$ T), $H_{c2}(T)$ undergoes a clear change in curvature, which coincides with $\mu_0 H_{c2}^* = 0.96$ T of the first superconducting band (see figure 8). The remarkable agreement of the TB model with the experimental data across the full temperature range is clearly seen in figure 10, from which we find $\mu_0 H_{c2}^{TB}(0) = 2.0(2)$ T and $\xi(0) = 12.8(6)$ nm. Note that the T_c and $\mu_0 H_{c2}$ values of the spurious Mo₃P phase [22] are both much smaller than those of Mo₅PB₂. Consequently, the two-gap feature of $H_{c2}(T)$ is intrinsic to Mo₅PB₂. The lower critical field $\mu_0 H_{c1}$ is related to the magnetic penetration depth λ and the coherence length ξ via $\mu_0 H_{c1} = (\Phi_0/4\pi\lambda^2)[\ln(\kappa) + 0.5]$, where $\kappa = \lambda/\xi$ is the GL parameter [36]. By using $\mu_0 H_{c1} = 30.4(4)$ mT and $\mu_0 H_{c2} = 2.0(2)$ T, the resulting magnetic penetration depth $\lambda_{GL} = 122(2)$ nm, is almost identical

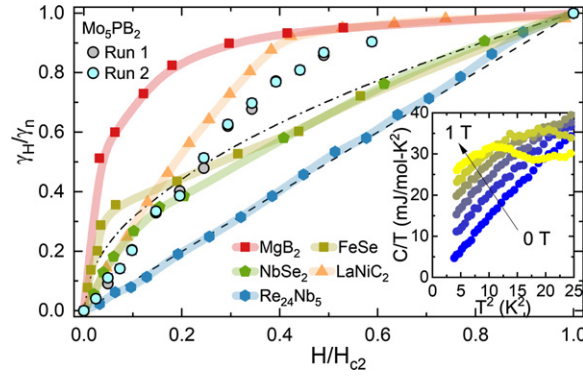


Figure 11. Normalized specific-heat coefficient γ_H/γ_n vs reduced magnetic field $H/H_{c2}(0)$ for Mo_5PB_2 . At a given applied field, γ_H is obtained as the linear extrapolation of C/T vs T^2 in the superconducting state to zero temperature (see inset). The dashed and dash-dotted lines represent the $\gamma(H)$ expected for a single-gap model with isotropic or line nodal gap structure, respectively. The data for the reference samples are adopted from references [49–53].

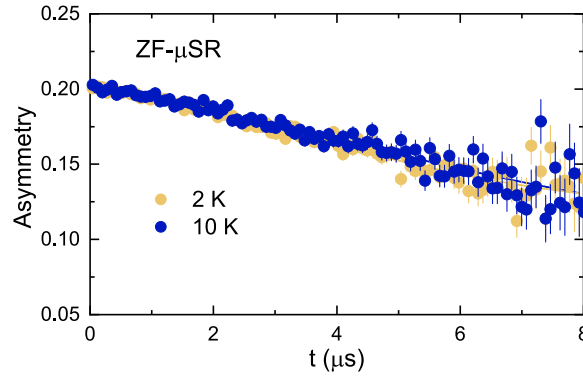


Figure 12. Representative ZF- μSR spectra in the normal (10 K) and the superconducting state (2 K) of Mo_5PB_2 . Solid lines are fits to the equation described in the text. None of the datasets shows noticeable changes with temperature.

to the experimental value 121(2) nm determined from TF- μSR data (see section 3.5). A large GL parameter, $\kappa \sim 9.5$, clearly indicates that Mo_5PB_2 is a type-II superconductor.

γ_H vs H . The multigap SC of Mo_5PB_2 is further confirmed by the field-dependent electronic specific heat coefficient $\gamma_H(H)$. Since the virtual $\mu_0 H_{c2}^*$ corresponds to the critical field which suppresses the small superconducting gap, we expect also $\gamma_H(H)$ to change its slope around $\mu_0 H_{c2}^*$. The normalized γ_H/γ_n values vs the reduced magnetic field $H/H_{c2}(0)$ are shown in figure 11 (here γ_n is the zero-field normal-state value). Note that, the field dependence of γ_H/γ_n measured at 0.4 K exhibits similar features to that evaluated at zero temperature. For Mo_5PB_2 , $\gamma_H(H)$ clearly deviates from the linear field dependence expected for fully-gapped superconductors with a single gap, as e.g., $\text{Re}_{24}\text{Nb}_5$ (dashed line) [52, 54], or from the square-root dependence \sqrt{H} (dash-dotted line), expected for nodal superconductors [55, 56]. Instead, Mo_5PB_2 exhibits similar features to other well known multigap superconductors, as e.g., FeSe [51], MgB_2 [49], or NbSe_2 [53]. The $\gamma_H(H)$ curve of Mo_5PB_2 (scatter plot) exhibits a significant change of slope around $H/H_{c2}(0) \sim 0.45$ (i.e., $\mu_0 H \sim 0.9$ T), which is highly consistent with $\mu_0 H_{c2}^*$.

3.7. Zero-field μSR

We also performed ZF- μSR measurements in both the normal- and the superconducting states of Mo_5PB_2 . As shown in figure 12, neither coherent oscillations nor fast decays could be identified in the spectra collected above (12 K) and below T_c (2 K), hence implying the lack of any magnetic order or fluctuations. The weak muon-spin relaxation in absence of an external magnetic field is mainly due to the randomly oriented nuclear moments, which can be modeled by a Gaussian Kubo–Toyabe relaxation function,

$G_{\text{KT}} = [\frac{1}{3} + \frac{2}{3}(1 - \sigma_{\text{ZF}}^2 t^2) e^{-\sigma_{\text{ZF}}^2 t^2/2}]$ [31, 57]. Here, σ_{ZF} is the zero-field Gaussian relaxation rate. The solid lines in figure 12 represent fits to the data by considering also an additional zero-field Lorentzian relaxation Λ_{ZF} , i.e., $A_{\text{ZF}}(t) = A_s G_{\text{KT}} e^{-\Lambda_{\text{ZF}} t} + A_{\text{bg}}$. The relaxations in the normal- and the superconducting states are almost identical, as confirmed by the practically overlapping ZF- μSR spectra above and below T_c .

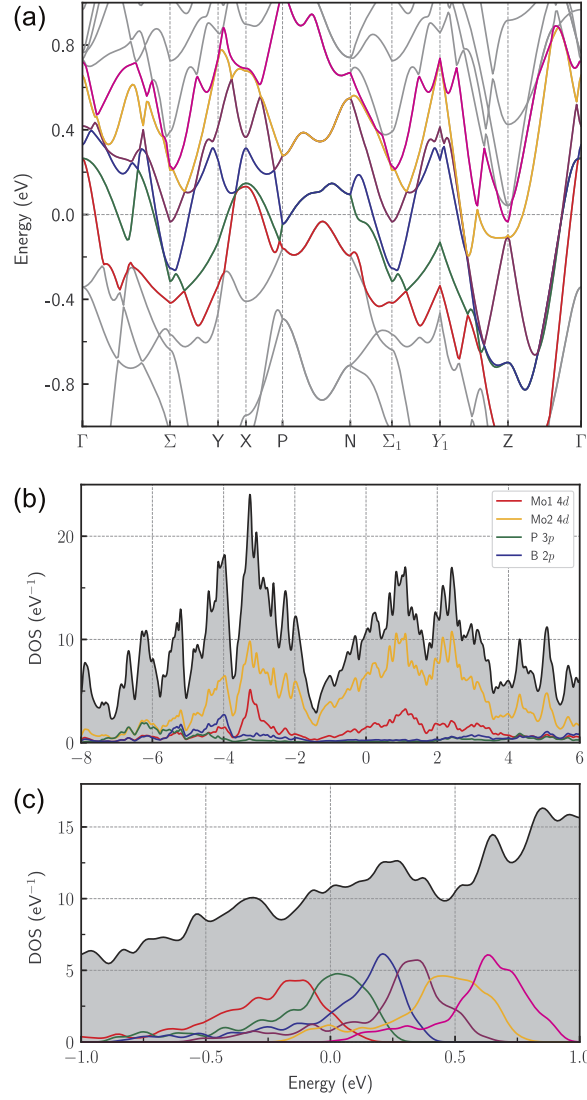


Figure 13. (a) Electronic band structure of Mo_5PB_2 , calculated by ignoring the spin–orbit coupling. The various bands which cross the Fermi level are plotted in different colors. Total- and partial density of states near the Fermi level for (b) different atoms and (c) the six different bands.

This lack of evidence for an additional μSR relaxation below T_c excludes a possible time-reversal symmetry breaking in the superconducting state of Mo_5PB_2 .

3.8. Electronic band-structure calculations and discussion

Apart from the zero-field electronic specific heat (see figure 7 and reference [11]), at a microscopic level, the multigap superconductivity of Mo_5PB_2 was also probed by field-dependent μSR relaxation $\sigma_{\text{sc}}(H)$ in the superconducting state (figure 8). Macroscopically, further evidence was brought by the temperature-dependent upper critical field $\mu_0 H_{c2}(T)$ (figure 10) and the field-dependent electronic specific heat coefficient $\gamma_{\text{H}}(H)$ (figure 11). Our data clearly indicate that Mo_5PB_2 is a multiband superconductor with two distinct superconducting gaps, both opening below T_c . Although extraneous phases, such as Mo_3P , might potentially influence the reported results, we found that their influence is negligible (both qualitatively and quantitatively). Below we show that the multigap SC is also supported by electronic band-structure calculations.

As can be seen in figure 13, six different bands are identified to cross the Fermi level. Among these, bands 1 (red-), 2 (green-) and 3 (blue line), all stemming primarily from the Mo 4d orbitals, contribute significantly to the density of states at the Fermi level (see table 1). We expect the multiband features of Mo_5PB_2 to be closely related to the different site symmetries of Mo atoms in the unit cell, namely, Mo1 (4c) and Mo2 (16l). According to band-structure calculations, the contribution of 16l-Mo atoms to the DOS is preponderant compared to that of 4c-Mo atoms [see figure 13(b)]. The Fermi velocities v_F of these bands,

Table 1. Calculated Fermi velocity v_F for the different bands near the Fermi level and the band contributions to the total DOS. Here v_F is in 10^5 m s^{-1} units.

Index	DOS (%)	v_F ($\Gamma-X$)				v_F ($\Gamma-Z$)
1	19.72	5.82	6.39	—	—	7.92
2	42.84	2.59	8.03	3.48	2.61	5.32
3	18.58	—	—	5.29	4.43	5.32
4	7.35	—	—	2.89	2.10	7.05
5	10.86	—	—	—	—	2.88
6	0.48	—	—	—	—	5.49

Table 2. Normal- and superconducting-state properties of Mo_5PB_2 . The London penetration depth λ_L , effective mass m^* , carrier density n_s , BCS coherence length ξ_0 , electronic mean-free path l_e , Fermi velocity v_F , and effective Fermi temperature T_F are also listed.

Property	Value (uncert.)	Property	Value (uncert.)
T_c^a	9.20(2) K	$\mu_0 H_{c2}$	2.0(2) T
ρ_0	41.1(2) $\mu\Omega \text{ cm}$	$\mu_0 H_{c2}^b$	0.96(5) T
Θ_D^R	236(5) K	$\xi(0)$	12.8(6) nm
$\mu_0 H_{c1}$	30.4(4) mT	κ	9.5(5)
$\mu_0 H_{c1}^{\mu\text{SR}}$	30.8(6) mT	λ_0	121(2) nm
γ_n	22.3(2) $\text{mJ mol}^{-1} \text{ K}^{-2}$	λ_0^b	99(2) nm
Θ_D^C	300(5) K	λ_{GL}	122(2) nm
Θ_E^C	530(5) K	λ_L	54(4) nm
Δ_0 (p -wave) (μSR)	1.87(2) meV	l_e	8.4(6) nm
Δ_0 (d -wave) (μSR)	1.76(2) meV	ξ_0	34.2(6) nm
Δ_0 (s -wave) (μSR)	1.42(1) meV	m^*	5.7(5) m_e
w	0.25	n_s	$5.9(7) \times 10^{28} \text{ m}^{-3}$
Δ_0^f (μSR) ^c	1.11(2) meV	v_F	$2.3(2) \times 10^5 \text{ ms}^{-1}$
Δ_0^s (μSR) ^c	1.57(1) meV	T_F	$2.1(2) \times 10^4 \text{ K}$
$\Delta_0^f(C)$ ^c	1.02(2) meV		
$\Delta_0^s(C)$ ^c	1.49(2) meV		

^aSimilar values were determined via electrical resistivity, magnetic susceptibility, and heat-capacity measurements.

^bDerived from a two-band-model fit to $\sigma_{\text{FLL}}(H)$ at 1.5 K.

^cDerived from a two-gap model analysis.

calculated along the $\Gamma-X$ and $\Gamma-Z$ directions, are summarized in table 1. Considering also the relative weights, the average v_F is comparable to the experimental value (see table 2).

The deviation of $\sigma_{\text{sc}}(H)$ (figure 8) from a single-band model and the appearance of an upward curvature in the upper critical-field data (figure 10), both reflect the occurrence of two distinct coherence lengths for two different bands, here leading to distinct upper critical fields. The Ginzburg–Landau coherence length determined from the upper critical field, $\xi(0) = \sqrt{\Phi_0/(2\pi H_{c2})}$, is proportional to the BCS coherence length ξ_0 , i.e., $\xi(0) = 0.855\sqrt{\xi_0 l_e}$ [37]. At zero temperature, the BCS coherence length is also related to the superconducting energy gap Δ_0 and the Fermi velocity v_F , i.e., $\xi_0 = \hbar v_F/\pi \Delta_0$. Therefore, for a multigap superconductor such as Mo_5PB_2 , $v_F^f/v_F^s = \xi_0^f/\xi_0^s \Delta_0^s/\Delta_0^f$. According to the zero-field electronic specific-heat results, $\Delta_0^f/\Delta_0^s = 1.02/1.49$, while the analysis of $\sigma_{\text{sc}}(H)$ with a two-band model yields $\xi^f(1.5 \text{ K}) = 18.5(5) \text{ nm}$ and $\xi^s(1.5 \text{ K}) = 13.2(2) \text{ nm}$. Assuming $\xi^f/\xi^s = \xi_0^f/\xi_0^s$, we find $v_F^f/v_F^s = 0.95$, which is highly consistent with the theoretical estimates reported in table 1. For instance, along the $\Gamma-Z$ direction, the dominant bands (1, 2, and 3) show very similar v_F values.

4. Conclusion

In summary, we studied the multigap superconductor Mo_5PB_2 by means of electrical resistivity, magnetization, heat capacity, and μSR , as well as via numerical calculations. The temperature dependence of the zero-field electronic specific heat and superfluid density reveal a nodeless superconductivity, well described by an isotropic s -wave model. The multigap features, originally inferred from zero-field specific-heat data are here further supported by the field-dependent electronic specific-heat coefficient and the superconducting Gaussian relaxation rate, as well as by the temperature dependence of the upper critical field. The lack of spontaneous magnetic fields below T_c indicates that time-reversal symmetry is preserved in the superconducting state of Mo_5PB_2 . By combining the extensive experimental results

presented here with numerical band-structure calculations, we provide solid evidence for the multigap superconductivity in Mo₅PB₂.

Acknowledgments

The authors thank Chien-Lung Huang from Rice University for fruitful discussions and acknowledge the assistance from the S μ S beamline scientists. This work was supported by the Schweizerische Nationalfonds zur Förderung der Wissenschaftlichen Forschung, SNF (Grants No. 200021_169455 and 206021_139082).

ORCID iDs

T Shang  <https://orcid.org/0000-0002-5916-0020>
D J Gawryluk  <https://orcid.org/0000-0003-4460-7106>
H Q Yuan  <https://orcid.org/0000-0002-9787-4884>
T Shiroka  <https://orcid.org/0000-0001-8624-2649>

References

- [1] Bormio-Nunes C, Nunes C A, Coelho A A, Faria M I S T, Suzuki P A and Coelho G C 2010 *J. Alloys Compd.* **508** 5
- [2] de Almeida D M, Bormio-Nunes C, Nunes C A, Coelho A A and Coelho G C 2009 *J. Magn. Magn. Mater.* **321** 2578
- [3] Xie Z G, Geng D Y and Zhang Z D 2010 *Appl. Phys. Lett.* **97** 202504
- [4] McGuire M A and Parker D S 2015 *J. Appl. Phys.* **118** 163903
- [5] Lamichhane T N, Taufour V, Thimmaiah S, Parker D S, Bud'ko S L and Canfield P C 2016 *J. Magn. Magn. Mater.* **401** 525
- [6] Brauner A, Nunes C A, Bortolozo A D, Rodrigues G and Machado A J S 2009 *Solid State Commun.* **149** 467
- [7] Machado A J S, Costa A M S, Nunes C A, Dos Santos C A M, Grant T and Fisk Z 2011 *Solid State Commun.* **151** 1455
- [8] Fukuma M, Kawashima K, Maruyama M and Akimitsu J 2011 *J. Phys. Soc. Japan* **80** 024702
- [9] Fukuma M, Kawashima K and Akimitsu J 2012 *Phys. Procedia* **27** 48
- [10] Corrêa L E, da Luz M S, de Lima B S, Cigarroa O V, da Silva A A P, Coelho G C, Fisk Z and Machado A J S 2016 *J. Alloys Compd.* **660** 44
- [11] McGuire M A and Parker D S 2016 *Phys. Rev. B* **93** 064507
- [12] Amato A, Luetkens H, Sedlak K, Stoykov A, Scheuermann R, Elender M, Raselli A and Graf D 2017 *Rev. Sci. Instrum.* **88** 093301
- [13] Suter A and Wojek B M 2012 *Phys. Procedia* **30** 69
- [14] Perdew J P, Burke K and Ernzerhof M 1996 *Phys. Rev. Lett.* **77** 3865
- [15] Kresse G and Furthmüller J 1996 *Phys. Rev. B* **54** 11169
- [16] Kresse G and Furthmüller J 1996 *Comput. Mater. Sci.* **6** 15
- [17] Kresse G and Joubert D 1999 *Phys. Rev. B* **59** 1758
- [18] Blöchl P E 1994 *Phys. Rev. B* **50** 17953
- [19] Rodríguez-Carvajal J 1993 *Physica B: Condens. Matter* **192** 55
- [20] Ziegler W T and Young R A 1953 *Phys. Rev.* **90** 115
- [21] Matthias B T and Hulm J K 1952 *Phys. Rev.* **87** 799
- [22] Shang T *et al* 2019 *Phys. Rev. B* **99** 184513
- [23] Bloch F 1930 *Z. Phys.* **59** 208
- [24] Blatt F J 1968 *Physics of Electronic Conduction in Solids* (New York: McGraw-Hill) pp 185–90
- [25] Mott N F and Jones H 1958 *The Theory of the Properties of Metals and Alloys* (Oxford: Oxford University Press)
- [26] Mott N F 1964 *Adv. Phys.* **13** 325–403
- [27] Tari A 2003 *The Specific Heat of Matter at Low Temperatures* (London: Imperial College Press)
- [28] Rajpoot P, Rastogi A and Verma U P 2018 *Phil. Mag.* **98** 422
- [29] Aharoni A 1998 *J. Appl. Phys.* **83** 3432
- [30] Osborn J A 1945 *Phys. Rev.* **67** 351
- [31] Yaouanc A and de Réotier P D 2011 *Muon Spin Rotation, Relaxation, and Resonance: Applications to Condensed Matter* (Oxford: Oxford University Press)
- [32] Amato A 1997 *Rev. Mod. Phys.* **69** 1119
- [33] Blundell S J 1999 *Contemp. Phys.* **40** 175
- [34] Maisuradze A, Khasanov R, Shengelaya A and Keller H 2009 *J. Phys.: Condens. Matter* **21** 075701 (and references therein)
- [35] Barford W and Gunn J M F 1988 *Physica C* **156** 515
- [36] Brandt E H 2003 *Phys. Rev. B* **68** 054506
- [37] Tinkham M 1996 *Introduction to Superconductivity* 2nd edn (New York: Dover)
- [38] Carrington A and Manzano F 2003 *Physica C* **385** 205
- [39] Khasanov R, Amato A, Biswas P K, Luetkens H, Zhigadlo N D and Batlogg B 2014 *Phys. Rev. B* **90** 140507(R)
- [40] Khasanov R, Gupta R, Das D, Leithe-Jasper A and Svanidze E 2020 *Phys. Rev. B* **102** 014514
- [41] Bouquet F, Wang Y, Fisher R A, Hinks D G, Jorgensen J D, Junod A and Phillips N E 2001 *Europhys. Lett.* **56** 856
- [42] Serventi S *et al* 2004 *Phys. Rev. Lett.* **93** 217003
- [43] Zhu X, Yang H, Fang L, Mu G and Wen H H 2008 *Supercond. Sci. Technol.* **21** 105001
- [44] Werthamer N R, Helfand E and Hohenberg P C 1966 *Phys. Rev.* **147** 295
- [45] Gurevich A 2011 *Rep. Prog. Phys.* **74** 124501 and references therein
- [46] Müller K H, Fuchs G, Handstein A, Nenkov K, Narozhnyi V N and Eckert D 2001 *J. Alloys Compd.* **322** L10
- [47] Gurevich A *et al* 2004 *Supercond. Sci. Technol.* **17** 278
- [48] Nakajima Y, Hidaka H, Nakagawa T, Tamegai T, Nishizaki T, Sasaki T and Kobayashi N 2012 *Phys. Rev. B* **85** 174524

- [49] Bouquet F, Fisher R A, Phillips N E, Hinks D G and Jorgensen J D 2001 *Phys. Rev. Lett.* **87** 047001
- [50] Chen J, Jiao L, Zhang J L, Chen Y, Yang L, Nicklas M, Steglich F and Yuan H Q 2013 *New J. Phys.* **15** 053005
- [51] Chen J T, Sun Y, Yamada T, Pyon S and Tamegai T 2017 *J. Phys.: Conf. Ser.* **871** 012016
- [52] Shang T *et al* 2018 *Phys. Rev. Lett.* **121** 257002
- [53] Huang C L, Lin J Y, Chang Y T, Sun C P, Shen H Y, Chou C C, Berger H, Lee T K and Yang H D 2007 *Phys. Rev. B* **76** 212504
- [54] Caroli C, De Gennes P G and Matricon J 1964 *Phys. Lett.* **9** 307
- [55] Volovik G E 1993 *JETP Lett.* **58** 469–73
- [56] Wen H H, Liu Z Y, Zhou F, Xiong J, Ti W, Xiang T, Komiya S, Sun X and Ando Y 2004 *Phys. Rev. B* **70** 214505
- [57] Kubo R and Toyabe T 1967 *A Stochastic Model for Low Field Resonance and Relaxation Magnetic Resonance and Relaxation* ed R Blinc (Amsterdam: North-Holland) p 810